



RESEARCH ARTICLE

10.1029/2020JB021489

Upward-Doming Zones of Gas Hydrate and Free Gas at the Bases of Gas Chimneys, New Zealand's Hikurangi Margin

Key Points:

- 240 m thick free gas column accumulated beneath the base of hydrate stability, which led to hydraulic fracturing and gas chimney formation
- Broad zone of free gas and gas hydrate formed beneath the gas chimney, extending upward from the regional base of hydrate stability
- Such zones of hydrate and free gas likely form due to pronounced lithological contrasts (sealing layers) within the hydrate stability zone

Supporting Information:

Supporting Information may be found in the online version of this article.

Correspondence to:

G. J. Crutchley,
gcrutchley@geomar.de

Citation:

Crutchley, G. J., Mountjoy, J. J., Hillman, J. I. T., Turco, F., Watson, S., Flemings, P. B., et al. (2021). Upward-doming zones of gas hydrate and free gas at the bases of gas chimneys, New Zealand's Hikurangi margin. *Journal of Geophysical Research: Solid Earth*, 126, e2020JB021489. <https://doi.org/10.1029/2020JB021489>

Received 11 DEC 2020

Accepted 8 SEP 2021

G. J. Crutchley¹ , J. J. Mountjoy² , J. I. T. Hillman³ , F. Turco⁴ , S. Watson² , P. B. Flemings⁵ , B. Davy³ , S. Woelz² , A. R. Gorman⁴ , and J. Bialas¹

¹GEOMAR Helmholtz Centre for Ocean Research Kiel, Kiel, Germany, ²National Institute of Water and Atmospheric Research, Wellington, New Zealand, ³GNS Science, Lower Hutt, New Zealand, ⁴University of Otago, Dunedin, New Zealand, ⁵Jackson School of Geosciences, University of Texas at Austin, Austin, TX, USA

Abstract Focused gas migration through the gas hydrate stability zone in vertical gas conduits is a global phenomenon. The process can lead to concentrated gas hydrate formation and seafloor gas seepage, which influences seafloor biodiversity and ocean biogeochemistry. However, much is unknown about how gas and gas hydrate co-exist within and around gas conduits. We present seismic imaging of the gas hydrate system beneath a four-way closure anticlinal ridge at New Zealand's southern Hikurangi subduction margin. Gas has accumulated beneath the base of gas hydrate stability to a thickness of up to ~240 m, which has ultimately led to hydraulic fracturing and propagation of a vertical gas conduit to the seafloor. Despite the existence of an array of normal faults beneath the ridge, these structures are not exploited as long-range gas flow conduits. Directly beneath the conduit, and extending upward from the regional base of gas hydrate stability, is a broad zone characterized by both negative- and positive-polarity reflections. We interpret this zone as a volume of sediment hosting both gas hydrate and free gas, that developed due to partial gas trapping beneath a mass transport deposit. Similar highly reflective zones have been identified at the bases of other gas conduits, but they are not intrinsic to all gas conduits through gas hydrate systems. We suggest that pronounced intervening sealing units within the gas hydrate stability zone determine whether or not they form.

Plain Language Summary Gas hydrates are ice-like substances composed of natural gas and water. They form between sediment grains underneath large regions of the Earth's seafloor. An important reason to study gas hydrates is that they partly control the way that methane gas flows through sediments and out of the seafloor. It is this flow of methane that sustains some diverse biological communities on the seafloor and affects the chemistry of the oceans. In this study, we use reflected sound waves to explore how gas flow beneath the seafloor depends on the way in which sedimentary layers are folded and fractured. Our data reveal a 240-m thick reservoir of gas that is trapped in a large sedimentary fold, ~500 m beneath the seafloor. The buoyancy of the gas has caused a vertical fracture zone to propagate upward to the seafloor, where gas bubbles are venting into the ocean. Further, our data suggest that a broad accumulation of gas hydrates (together with gas) has formed beneath the vertical fracture zone. This gas hydrate deposit may grow larger with time, and it will continue to influence the way that gas flows through the sediments.

1. Introduction

Gas migration through the gas hydrate stability zone (GHSZ) is a widespread global phenomenon, with many examples having been documented from seismic reflection data, scientific drilling and modeling studies (Brooks et al., 1994; Flemings et al., 2003; Fu et al., 2020; Gorman et al., 2002; Liu & Flemings, 2006; Plaza-Faverola et al., 2011; Tréhu, Flemings, et al., 2004; Wood et al., 2002). A range of mechanisms have been invoked to explain free gas existence within the GHSZ, including factors that suppress the rate of hydrate formation or alter its thermodynamic stability (e.g., Clennell et al., 1999; Liu & Flemings, 2006), or rapid free gas transport rates that out-pace the rate of hydrate formation (e.g., Haeckel et al., 2004; Liu et al., 2019; Tréhu, Flemings, et al., 2004). The pathways of focused free gas flow are commonly referred to as “conduits”, “chimneys” or “pipes”, which often extend all the way to the seafloor. The focused flow influences gas hy-

© 2021. The Authors.

This is an open access article under the terms of the [Creative Commons Attribution License](https://creativecommons.org/licenses/by/4.0/), which permits use, distribution and reproduction in any medium, provided the original work is properly cited.

hydrate formation in the subsurface (e.g., Haeckel et al., 2004; Liu & Flemings, 2006; Liu et al., 2019), while the methane released at the seafloor has broad implications for marine biodiversity and ocean biogeochemistry (Biaostoch et al., 2011; Levin et al., 2016; MacDonald et al., 2003).

The driving force behind gas conduit formation is overpressure accumulation, where gas buoyancy from interconnected free gas columns beneath the base of the gas hydrate stability zone (BGHSZ) drives the system toward mechanical failure (e.g., Flemings et al., 2003; Tréhu, Flemings, et al., 2004). It is often unclear what extent focused free gas migration makes use of existing planes of weakness (shallow faults) versus the generation of new pathways formed by hydraulic fracturing (e.g., Finkbeiner et al., 2001; Flemings et al., 2003; Hornbach et al., 2004). In this sense, both faults and hydraulic fractures can be thought of as gas conduits if they provide pathways for focused upward gas migration.

Rapid free gas migration through to the seafloor has implications for gas hydrate formation styles. At South Hydrate Ridge, a broad zone of gas hydrate has formed from the free gas phase in the shallow sub-seafloor as a result of rapid gas transport (Haeckel et al., 2004; Tréhu, Flemings, et al., 2004). This zone of concentrated hydrate manifests itself in seismic reflection data as disrupted, high-amplitude reflectivity (Crutchley et al., 2013; Tréhu, Flemings, et al., 2004; Tréhu, Long, et al., 2004). In other cases, gas conduits are also cored by broader zones of high-amplitude reflectivity that extend upwards from the regional BGHSZ (e.g., Koch et al., 2016). The relationships between free gas and gas hydrate within such zones are not well understood.

In this study, we investigate the development of a gas conduit that has formed above a thick interconnected free gas column beneath a four-way closure anticlinal ridge. Using a combination of older low-frequency and recently acquired high-frequency seismic reflection data, we aim to:

1. Determine the broad geological controls on free gas accumulation and trapping beneath the ridge.
2. Constrain the thickness of interconnected free gas beneath the conduit and the approximate in-situ stress conditions within which the gas conduit developed.
3. Evaluate fault-controlled free gas migration versus vertical conduit formation.
4. Investigate the possible co-existence of gas hydrate and free gas in a zone of high reflectivity that extends upward from the regional BGHSZ, at the base of the conduit.

2. Geological Setting

Our study area lies at the southern end of New Zealand's Hikurangi subduction margin, where the Pacific Plate has been subducting beneath the Australian Plate (Figure 1a) since ~24–30 Ma (Ballance, 1976; Stern et al., 2006). Convergence is highly oblique in this region (DeMets et al., 2010, Figure 1b), which results in a tectonically complex transition zone between subduction and strike slip motion (Barnes et al., 1998; Wallace et al., 2012).

Bottom simulating reflections (BSRs) and methane seepage out of the seafloor are widespread on the Hikurangi margin (Barnes et al., 2010; Greinert et al., 2010; Katz, 1982; Watson et al., 2020). There is also widespread evidence from seismic reflection data for concentrated gas hydrate accumulations, particularly within dipping strata of anticlinal ridges that tend to focus fluid flow (e.g., Crutchley, Kroeger, et al., 2018; Fraser et al., 2016; Pecher & Henrys, 2003). Geochemical analyses point to a biogenic origin of methane for hydrate formation (Koch et al., 2016; Schwalenberg et al., 2010). Deep seismic imaging and modeling studies have suggested that thermogenic gas generation may also contribute to the formation of concentrated hydrate accumulations (Kroeger et al., 2015, 2019; Plaza-Faverola et al., 2012).

The ridge we are investigating in this study lies close to the deformation front of the wedge, ~2,100–2,300 m below sea level (mbsl) (Figure 1c). The ridge is a four-way closure anticline system, with its longest axis trending approximately northeast-southwest. Active free gas release into the water column near the crest of the ridge has been documented by Watson et al. (2020).

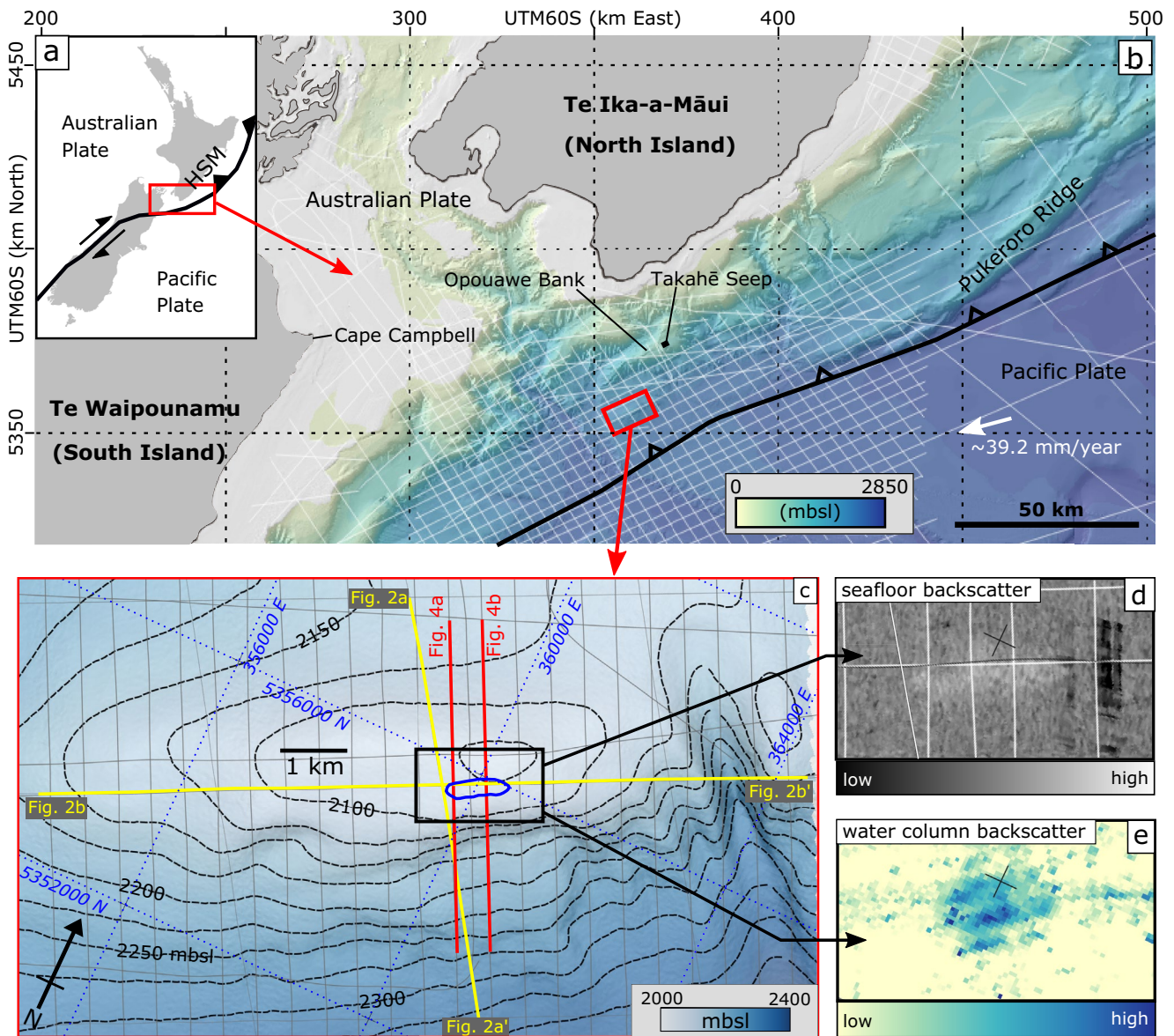


Figure 1. (a) Regional tectonic setting of New Zealand. Pacific Plate subducts obliquely beneath the Australian Plate at the Hikurangi subduction margin (HSM). Red box shows extent of map in (b), (b) The southern HSM. Approximate location of deformation front = bold toothed black line. Coordinate system = UTM60S, WGS84 datum (coordinates shown in km). Faint white lines = regional 2D seismic data. Location of the study area in this paper = red box. White arrow is the inter-plate vector (DeMets et al., 2010). Location of Takahē Seep site = black dot. (c) Enlarged study area map, rotated 25° clockwise. Coordinate system = UTM60S (meters), WGS84 datum. Contours = meters below sea level. Yellow and red lines show locations of seismic sections in subsequent figures. Pale gray lines show all seismic lines collected across this ridge. Blue polygon near ridge crest = region of elevated seafloor backscatter, marking long-term gas seepage. (d) The ridge-parallel patch of high seafloor backscatter (light gray region) at the crest of the ridge. (e) Elevated water column backscatter energy. Note: areal extent of this map is the same as (d).

3. Data and Observations

3.1. Multibeam Echo-Sounder Data

We collected multibeam bathymetry data and water column imaging data with a hull-mounted Kongsberg Maritime EM302 multibeam echo-sounder during Research Voyage TAN1808, aboard *RV Tangaroa* in 2018. These data revealed a region of gas seepage at the seafloor, which manifests itself as an area of high seafloor backscatter (Figure 1d), possibly related to the formation of authigenic carbonate and/or seep fauna. We

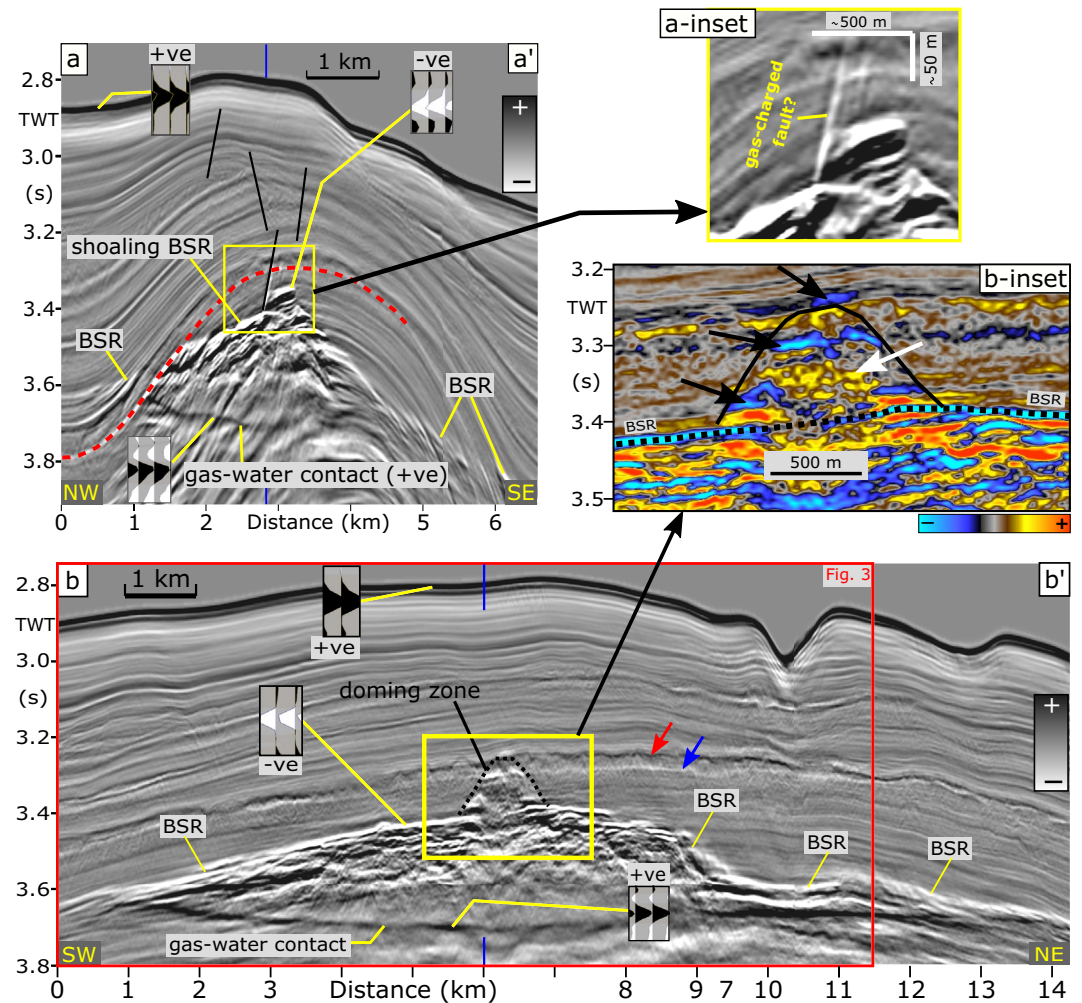


Figure 2. Lower-frequency seismic data (APB13 survey). (a-a') Ridge perpendicular section (Line APB13-32). See Figure 1c for location. Waveform polarity shown at selected locations. TWT = two-way time (s). Thin black lines = interpreted normal faults. Vertical blue lines = intersection with line (b-b'). Broken red line = base of a mass transport deposit (MTD) that is better imaged in high-frequency data in Figure 4. BSR = bottom simulating reflection. (a-inset) Enlarged plot from (a-a') showing a steeply dipping, linear, negative-polarity reflection that we interpret as a gas-charged fault plane reflection near the top of the shoaling BSR. (b-b') Ridge parallel section (Line APB13-25), with similar annotations to (a-a'). See Figure 1c for location. Red and blue arrows point to top and bottom (respectively) of the MTD. Vertical blue lines = intersection with line (a-a'). (b-inset) Enlarged color plot of a zone of doming reflectivity above the regional BSR level (see yellow box in (b-b') for location). Black arrows point to negative polarity events. White arrow points to zone of diffuse, positive polarity, high-amplitude reflectivity.

have also produced a vertical stack of multibeam water column data to reveal the region of active methane release into the water column (Figure 1e).

3.2. Long-Offset (Low-Frequency) Seismic Data

Two long-offset seismic lines, approximately orthogonal to each other, cross the crest of the ridge (Figure 1c, yellow lines). These lines (Sections 2a-2a' and 2b-2b', Figures 2a and 2b, respectively) are from the APB13 survey collected in 2013 by Anadarko New Zealand Company and processed by CGG Services Ltd. (Anadarko New Zealand Ltd, 2014). The data were collected with an 8 km-long streamer and a 3,610 in³ (~59 litre) airgun array. CGG Services Ltd. carried out a comprehensive seismic processing flow, including de-bubble and zero phase de-signature, various noise attenuation approaches, de-ghosting, de-multiple and Kirchhoff pre-stack time migration. Their final sections have a dominant frequency in the range of

10–20 Hz. Further details about the acquisition parameters and the processing flow are provided in the Supporting Information S1. For display purposes in this paper, we have flipped (180° phase rotation) the polarity of the seismic sections such that they conform with the American polarity convention, where an increase in acoustic impedance leads to a positive polarity peak in the seismic data (Brown & Abriel, 2014). This is demonstrated by the inset wavelets from the seafloor in Figures 2a and 2b. Wavelet shaping has resulted in a clean peak for the seafloor reflection, with only very minor negative polarity side lobes.

In addition to showing the migrated seismic sections as processed by CGG Services Ltd. (Figures 2a and 2b; Anadarko New Zealand Ltd, 2014), we carried out our own basic re-reprocessing of Section 2b-2b' (Figure 2b). The sole aim of our re-processing was to generate seismic interval velocities in the shallow sub-seafloor for this line, which were not otherwise available to us but are useful for investigating the gas hydrate system. Our re-processing included crooked line geometry definition, band pass filtering (frequencies of 5, 15, 100, and 150 Hz), Kirchhoff pre-stack time migration and semblance-based seismic velocity analysis on the pre-stack time migrated gathers. We converted the root-mean-square stacking velocities to interval velocities using the standard Dix equation (Dix, 1955), which is appropriate in the case of near flat-lying seismic reflectors. The most steeply dipping reflections that constrained our analysis on Section 2b-2b' dip at 3° , and most reflections have a dip of less than 2° .

3.2.1. Bottom Simulating Reflections and Gas-Water Contacts

The low-frequency seismic data reveal a prominent negative-polarity (opposite to seafloor polarity) BSR (Figures 2a and 2b), marking the BGHSZ in sediments. In these data, the BSR shoals toward the seafloor close to the apex of the anticlinal structure, with four-way closure that mimics the elongated bathymetry of the ridge. A linear, steeply dipping event occurs above the shoaling BSR near the apex of the anticline (Figure 2a-inset). Based on local seismic velocities, we estimate the dip of this event to be $\sim 40^\circ$, which is within the dip range of steeply dipping stratigraphic reflections observed on the limbs of anticlines elsewhere in this data set. This demonstrates that the linear event may be a properly imaged reflection; its negative polarity suggests that it may be a reflection from a free gas-charged fault. However, we cannot rule out the possibility that the event is an out-of-plane reflection or diffracted energy from a nearby zone of enhanced reflectivity (i.e., the “doming zone” labeled in Figure 2b and described in Section 3.2.2).

The low-frequency data also reveal a clear, positive-polarity gas-water contact (Figures 2a and 2b). Gas-water contacts like these have been observed elsewhere on the southern Hikurangi margin (Crutchley, Kroeger, et al., 2018; Fraser et al., 2016). The seismic signal is significantly attenuated ~ 100 – 200 ms beneath the BSR, but there is sufficient energy to return a coherent reflection from the gas-water contact at the base of the gas reservoir (Figures 2a and 2b). Our seismic velocity analysis on Line 2b-2b' resulted in the interval velocities shown in Figure 3a. The velocity model clearly reveals low velocities indicative of gas-charged sediments beneath the BSR (e.g., Fraser et al., 2016; Gorman et al., 2002; Singh et al., 1993), with velocities increasing again beneath the gas-water contact. The low velocities between the BSR and the gas-water contact are the reason for the non-horizontal appearance of the gas-water contact; it is a velocity “push down” effect (e.g., Chadwick et al., 2019).

3.2.2. Zone of Upward-Doming Reflectivity: Above the Regional BSR and Below a Mass-Transport Deposit

A distinct upward-doming zone of high-reflectivity exists above the regional BSR level in the centre of Section 2b-2b' (see Figure 2b-inset). We hereafter use the term “doming zone” to refer to this feature. Note that our usage of this term describes the spatial distribution of elevated seismic reflectivity related to gas and/or gas hydrate distribution, and not to any local doming of stratigraphy.

The doming zone in Section 2b-2b' is characterized by localized negative polarity reflections indicative of free gas accumulations (Figure 2b-inset, black arrows), as well as a more diffuse background zone of positive polarity reflections (Figure 2b-inset, white arrow). The diffuse region of positive polarity has distinctly higher amplitudes than the sediments surrounding the doming zone. Our velocity analysis through the doming zone indicates that it is a high-velocity zone, compared to the low velocities beneath the regional BSR level (Figure 3a). An example extraction of the semblance spectra (Figure 3b) shows the clear increase in root-mean-square velocities from the top of the doming zone to the BSR level.

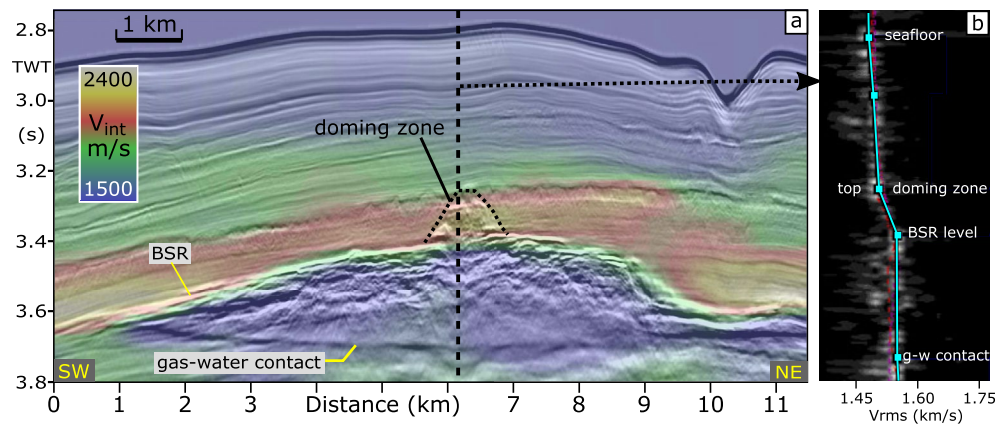


Figure 3. Lower-frequency seismic data (APB13 survey). (a) Ridge parallel section (Line APB13-25), from Figure 2b. TWT = two-way time (s). Some annotations from Figure 2b are included: BSR = bottom simulating reflection. Semi-transparent color overlay shows interval velocities (V_{int}) (m/s) from semblance-based seismic velocity analysis. (b) Example semblance spectrum at a location through the doming zone (location shown by vertical broken black line in (a)). Vertical scale identical to (a). Black = low semblance, white = high semblance. Picked semblance peaks from the seafloor, the top of the doming zone, the BSR level and the gas-water contact are shown. The velocity clearly increases from the top of the doming zone to the BSR.

The doming zone is capped by a unit of chaotic reflectivity with an irregular upper surface (red arrow, Figure 2b), a typical seismic manifestation of a mass transport deposit (MTD) (e.g., Sawyer et al., 2009). This MTD, and its relationship to the doming zone, is more clearly imaged in high-frequency seismic data (Section 3.3).

3.3. High-Frequency Seismic Data

During Research Voyage TAN1808 we collected a dense grid of 2D seismic lines (gray lines in Figure 1c) over the ridge to complement the lower-frequency imaging of the gas hydrate system. The data were acquired with a much shorter streamer than the APB13 survey, which precludes seismic velocity analysis. However, the advantage of the TAN1808 data is that they were acquired with a much smaller seismic source (150 in³, or ~2.46 litres) that delivered a significantly higher dominant frequency (~60–100 Hz), which enables higher-resolution imaging of the sub-seafloor (Figure 4). The acquisition parameters are provided in the Supporting Information S1 and in Crutchley, Mountjoy, et al. (2018). Our processing included: (a) crooked line geometry definition, (b) bandpass filtering (Butterworth filter with corner frequencies of 12, 24, 300, and 400 Hz), (c) automatic de-spiking and frequency-wavenumber (FK) filtering in the shot domain, (d) common-midpoint sorting and normal moveout (NMO) correction, and (e) 2D Stolt migration. The NMO correction and migration were carried out using a constant velocity of 1,500 m/s. As with the long-offset seismic data (Section 3.2), we applied a 180° phase rotation to the stacked sections of Crutchley, Mountjoy, et al. (2018) to conform with American polarity, so that a reflection from an increase in impedance is marked by a positive polarity waveform. This is demonstrated by the inset wavelets from the seafloor reflection in Figures 4a and 4b, where the strongest amplitude in the waveform is the positive (black) peak. Our interpretations of reflection polarity in the high-frequency data are based upon observing the dominant part of the waveform (negative or positive), as compared to the seafloor wavelet.

3.3.1. High-Frequency Seismic Manifestations of the Gas Hydrate System

As is known from studies elsewhere, gas hydrate systems manifest themselves very differently depending on seismic acquisition frequency (e.g., Berndt et al., 2019; Haines et al., 2017; Vanneste et al., 2001). The laterally coherent BSRs imaged in Section 2b-2b' (Figure 2b), for example, are not prevalent in the high-frequency data shown in Figures 4a and 4b. A faint BSR is apparent in places, but for the most part we interpret the upper limit of strong reflectivity as the seismic manifestation of the BGHSZ (Figures 4a and 4b), which correlates with the depth of BSRs in the low-frequency data. Negative polarity wavelet examples at this upper limit of strong reflectivity are shown in Figures 4a and 4b.

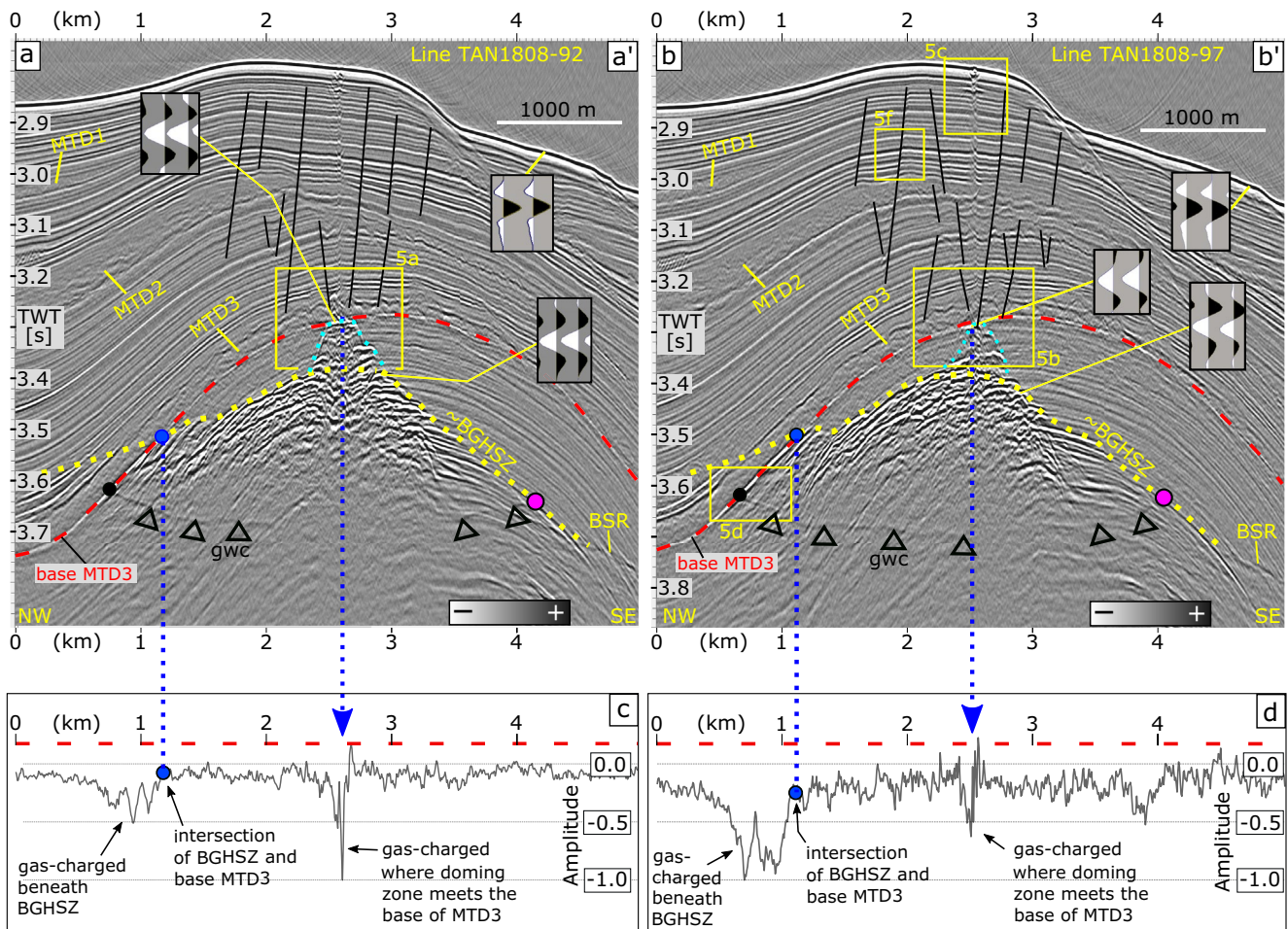


Figure 4. Higher-frequency seismic data (TAN1808 survey). (a-a') Seismic line TAN1808-92 (see Figure 1c for location). Black lines = normal faults. Wavelet insets show polarity at selected locations. Dotted yellow line = interpreted base of gas hydrate stability zone (BGHSZ), also constrained by crossing lines. Dotted cyan line = doming zone, extending up from the regional BGHSZ. Black triangles = gas-water contact (gwc). MTD = mass transport deposit. Note: MTD3 is the same MTD as that shown by the red and blue arrows in Figure 2b. Broken red line = base of MTD3. Blue dot = intersection of base MTD3 with BGHSZ. Black dot = intersection of gwc with base MTD3. Magenta dot = intersection of gwc with BGHSZ. Yellow boxes = enlargements shown in Figure 5. (b-b') Seismic line TAN1808-97 (see Figure 1c for location). Annotations as in (a-a'). (c) Normalized amplitudes along base MTD3, from Line TAN1808-92 (horizontal scale identical to (a-a')). Broken red line represents the 5 km horizontal distance along the base of MTD3. Blue dot = intersection with the BGHSZ. Blue arrow points to high amplitudes where gas is trapped beneath MTD3 at the apex of folding. (d) Normalized absolute amplitudes along base MTD3 (broken red line in (b-b')), from Line TAN1808-97 (horizontal scale identical to (b-b')). Annotations as in (c).

The high-amplitude doming zone identified in Section 2b-2b' (Figures 2b and 2b-inset) is also evident in the high frequency data (Figures 4a, 4b, 5a, and 5b). As in Section 2b-2b' (Figure 2b-inset), the high-frequency data reveal complex/disrupted reflectivity, with examples of both negative polarity and positive polarity reflections within this zone (Figure 5e). The gas-water contact reflection is also apparent in the high-frequency data (Figures 4a, 4b, and 5d). Although it is subtler than in the low-frequency data, it can be traced broadly throughout the network of seismic lines.

3.3.2. Mass Transport Deposits and 3D Structural Relationships

MTDs are identified in seismic data based on their chaotic and generally low-reflectivity appearance. The TAN1808 data image several MTDs that are interbedded within the continuous stratigraphic reflections beneath the ridge (Figures 4a and 4b). Amplitudes extracted along the base of the deepest MTD (MTD3) highlight the occurrence of free gas beneath this unit. For example, strong negative polarity amplitudes occur along the base of MTD3 in the region where it occurs beneath the regional BGHSZ (Figures 4c and 4d). Likewise, negative spikes in the amplitude at the base of MTD3 occur at the apex of folding, where the

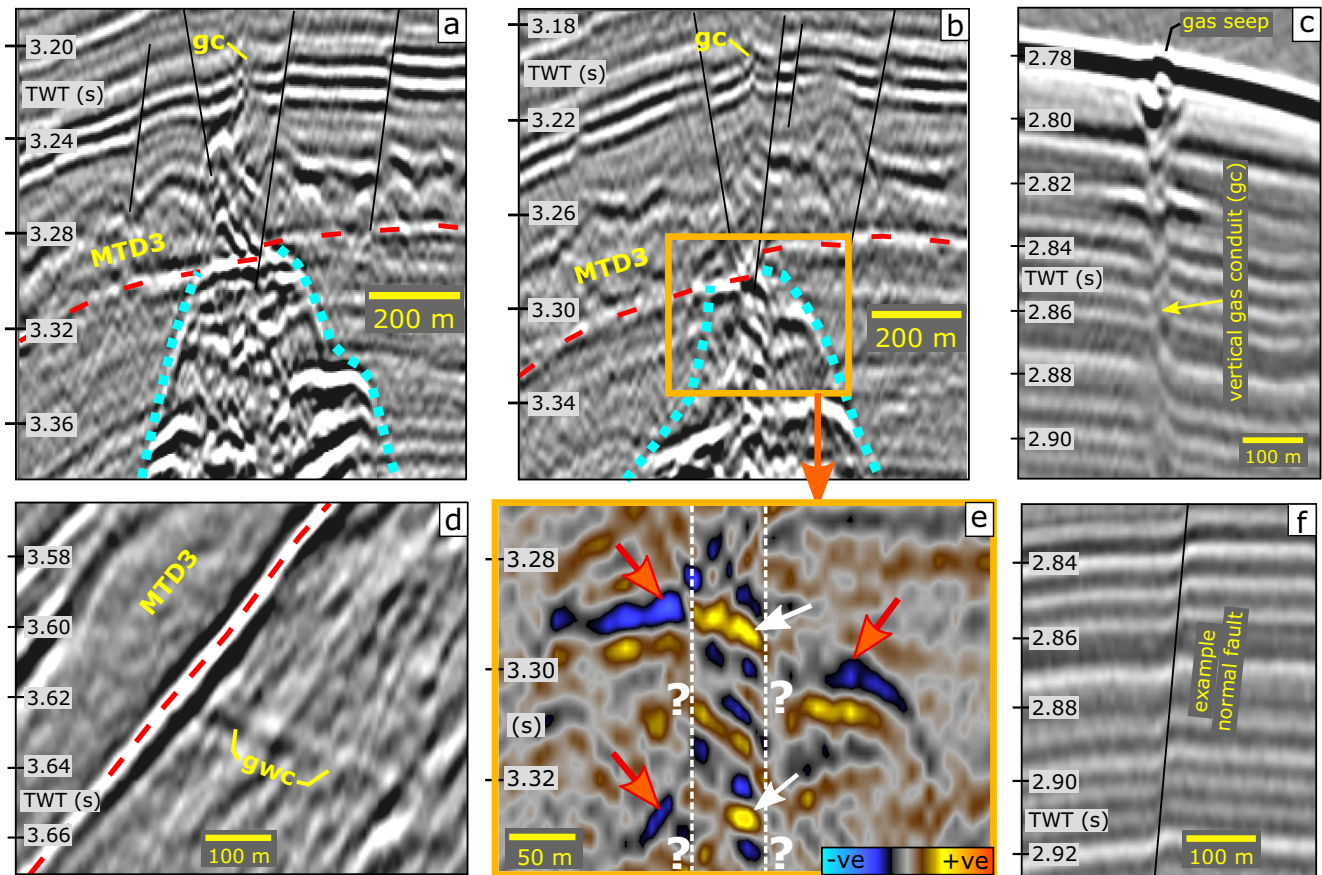


Figure 5. Enlargements from selected regions of Figures 4a and 4b (higher-frequency seismic data (TAN1808 survey)). (a) The high-amplitude doming zone in Line TAN1808-92 (within dotted cyan lines). Base of Mass Transport Deposit 3 (MTD3) = broken red line (as in Figures 2 and 4). Solid black lines = normal faults. “gc” is the vertical gas conduit. (b) The high-amplitude doming zone in Line TAN1808-97. Annotations as in (a). Note: as in (a), the base of MTD3 has been offset by one of the normal faults. (c) Upper extent of the vertical gas conduit. (d) Enlargement showing intersections of gas-water contact (gwc) with MTD3. (e) Enlarged color display of reflections within the upper part of the high-amplitude doming zone from (b). Orange arrows point to negative-polarity events; white arrows point to positive-polarity events. Dotted white lines mark the approximate downward projection of the vertical gas conduit shown in (a–c). (f) Example normal fault.

upper limit of the doming zone coincides with the level of the base of MTD3 (Figures 4c and 4d). These local amplitude anomalies can be seen in Figures 5a and 5b.

The closely spaced seismic profiles enable us to map out key seismic reflections spatially, including the regional BGHSZ and the base of MTD3. These structural maps in two-way time (Figure 6) reveal: (a) the intersection of the base of MTD3 with the BGHSZ, (b) the intersection of the gas-water contact with the base of MTD3, and (c) the intersection of the gas-water contact with the BGHSZ. Projected on top of both maps is the extent of the seafloor gas seep, as determined from elevated seafloor backscatter (Figure 1d).

3.3.3. Gas Conduit Amid Extensional Normal Faults

Directly above the shallowest part of the high-amplitude doming zone is a vertical gas conduit that extends to the seafloor (Figures 4a, 4b, and 5a–5c), where seafloor backscatter is elevated (Figure 1d) and free gas escapes into the water column (Figure 1e). The gas conduit, striking SW-NE, lies directly beneath the region of seafloor seepage. The gas conduit is vertical (Figure 5c), as opposed to surrounding normal faults (Figures 4a, 4b, and 5f) that have typical apparent dips of $\sim 60^\circ$, based on depth conversion using representative sub-seafloor velocities from Section 2b-2b’ (Figure 2b). The normal faults extend through much of the GHSZ and some reach as deep as the upper limit of the high-amplitude doming zone, offsetting the base of MTD3 (Figures 4a, 4b, 5a, and 5b).

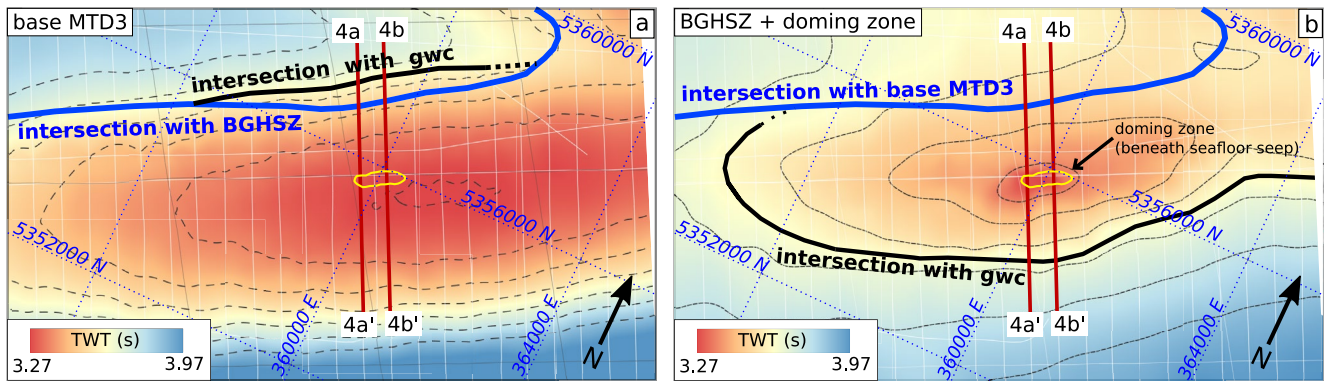


Figure 6. (a) Horizon map of base of Mass Transport Deposit 3 (MTD3), two-way time (TWT) in seconds (s). Red lines = locations of lines shown in (4a-4a') and (4b-4b'). Yellow polygon = seafloor seep site, from Figure 1d. Blue line = intersection with interpreted base of gas hydrate stability zone (BGHSZ). Black line = intersection with gas-water contact (gwc). Note, map extent is identical to that in Figure 1c: Coordinate system = UTM60S (meters), WGS84 datum. (b) Horizon map of BGHSZ, plus the doming zone that extends upward from the BGHSZ, in TWT (s). Map extent identical to (a). Blue line = intersection with base MTD3. Black line = intersection with gwc. Note: gas reservoir occurs between the black and blue lines, and also closes further to the northeast. Other annotations as in (a). Color bar identical to (a).

4. Discussion

4.1. Seismic Manifestations of Gas-Water Contacts Beneath Hydrate Systems

Gas-water contacts beneath gas hydrate systems commonly manifest themselves as relatively abrupt terminations of high reflectivity along dipping seismic reflections. “Horizon A” at South Hydrate Ridge on the Cascadia Margin is a well-documented example, where the down-dip termination of high reflectivity marks the gas-water contact within a succession of coarse-grained, ash-rich turbidite beds (Tréhu, Flemings, et al., 2004). Many other examples exist globally, including in relatively coarse-grained units in the Gulf of Mexico (e.g., Boswell et al., 2012). Another manifestation of the gas-water contact beneath hydrate systems is the “flat spot” – a sub-horizontal, positive polarity reflection marking the base of the free gas zone over broader lateral extents and across multiple dipping reflections (e.g., Amundsen et al., 2015; Crutchley, Kroeger, et al., 2018; Fraser et al., 2016; Rocha-Legorreta, 2009). The gas-water contact beneath the ridge in this current study falls into this latter category, indicating that free gas is distributed across a broad succession of dipping lithological units rather than being focused into a particular dipping unit. However, unlike the example presented by Amundsen et al. (2015), we do not observe multiple flat spots at different sub-sea-floor depths on the same seismic line. We interpret that the clearly defined flat spot (e.g., Figure 2b) records the base of a trapped interconnected column of free gas that extends laterally across strata and upward to the regional BGHSZ. The high amplitudes present and the fact that there is a single flat spot suggests that this gas reservoir is fairly homogenous and composed of rocks with a low capillary entry pressure, such as sand-rich reservoirs.

4.2. Seismic Reflection Evidence for Both Gas Hydrate and Free Gas Within the Doming Zone

The doming zone is a distinctive high seismic velocity zone, with velocities similar to (or slightly higher than) other regions directly above the BSR (Figure 3a) where gas hydrate is expected to exist. In clear contrast, the pronounced low velocity zone caused by free gas extends from the gas-water contact upward to the base of the doming zone–i.e., the regional BSR level (Figure 3a). In corroboration with the high seismic velocity character of the doming zone, the low-frequency data show that this zone contains diffuse, positive-polarity reflectivity that is stronger than the reflectivity of the surrounding sediments (Figure 2b-inset).

In addition to these observations supporting gas hydrate occurrence within the doming zone, the low frequency data also reveal strong, localized, negative-polarity reflections at the margins of the doming zone (Figure 2b-inset) that point to the existence of free gas. We infer that the free gas accumulations are too localized to be resolved by the semblance-based velocity analysis.

The high frequency data show both strong negative-polarity and positive-polarity reflections within the doming zone (Figure 5e). In summary, there are seismic reflection indicators in both the low-frequency and high-frequency data for both gas hydrate (positive polarity reflections) and free gas (negative polarity reflections) within the doming zone.

4.3. Lithological Seals and the Base of Gas Hydrate Stability

Our mapping of key seismic horizons reveals the importance of pronounced lithological contrasts in controlling the upper limit of free gas in sediments. The lithological contrast in this case is a buried MTD (“MTD3”, Figures 4a and 4b) that has been folded into the anticline together with the surrounding stratified sediments, and also offset locally by normal faults (Figures 5a and 5b). MTD3 appears to control the lateral extent of the free gas reservoir on the northwest side of the ridge; that is, the gas-water contact terminates laterally against the base of the folded MTD (Figure 5d), which is significantly deeper than the regional base of hydrate stability (Figures 4a and 4b). On the southeast side of the ridge, the gas-water contact truncates against the seaward-dipping BGHSZ, which lies well below the folded MTD (Figures 4a and 4b). Beneath the centre of the ridge, closer to the apex of folding, the MTD has again trapped free gas accumulations within the high-amplitude doming zone (Figures 5a and 5b).

MTD3 is therefore acting as an upper seal that limits the lateral and vertical extent of the gas reservoir. This is not surprising, since MTDs are typically characterized by densified sediment that have reduced pore throat diameters and enhanced capillary sealing (e.g., Day-Stirrat et al., 2013; Dugan, 2012; Sawyer et al., 2009; Sun et al., 2017). Indeed, the basal reflections of the three MTDs identified in Figures 4a and 4b are negative polarity, indicating a transition from high acoustic impedance within the MTDs (densified sediment) to lower acoustic impedance in the strata directly beneath the MTDs. The regions of anomalously high negative-polarity amplitudes along the base of MTD3 (e.g., Figures 4c and 4d) represent regions where free gas is trapped beneath the MTD. The free gas in these places leads to a local amplification of the inherent, lithology-derived impedance contrast.

The vertical extent of interconnected free gas, from the gas-water contact upwards, can be considered in relation to the approximate in-situ conditions for hydraulic fracturing at the base of the gas conduit. However, it is not immediately clear from the seismic data whether the gas conduit was initiated at the top of the high-amplitude doming zone (directly beneath MTD3), or whether it formed deeper in the stratigraphic succession—for example, approximately in line with the regional BSR level. To shed light on this, we investigate relationships between estimated sub-seafloor stress, gas buoyancy pressure, and hydraulic fracture criteria in the following section.

4.4. Mechanical Failure Conditions at the Base of the Gas Conduit

To understand the development of the gas hydrate system beneath this ridge requires that we explore the processes governing the movement of free gas into the GHSZ. This includes the flow of free gas across the regional BSR level and into the high-amplitude doming zone, as well as through MTD3 and upward toward the seafloor.

The regional BSR level beneath the gas conduit occurs at 3.38 s two-way time (TWT), i.e., 0.6 s beneath the seafloor (Figures 7a and 7b). The top of the doming zone occurs at 3.28 s TWT, i.e., 0.5 s beneath the seafloor (Figures 7a and 7b). We convert these times to depth below seafloor using the velocity model we generated along Section 2b-2b' (Figure 3a). Likewise, we estimate the thickness of the free gas zone between the gas-water contact and the regional BSR level using a velocity of 1,550 m/s, based on velocities from Section 2b-2b'. From these conversions we arrive at depths of ~435, ~540 and ~775 m below seafloor (mbsf) for the top of the doming zone, the regional BSR level and the gas-water contact, respectively (Figure 7c). We estimate an error of $\pm 5\%$ in our interval velocities, after converting from root-mean-square velocities, which is based on errors in picking semblance spectra. The percentage error accounts for increasing absolute error at higher velocities deeper beneath the seafloor. In the Supporting Information S2 we have carried out additional (conservative) analyses of potential velocity errors and how they propagate through to depth estimates of the key horizons named above. These analyses include a consideration of P-wave velocities from

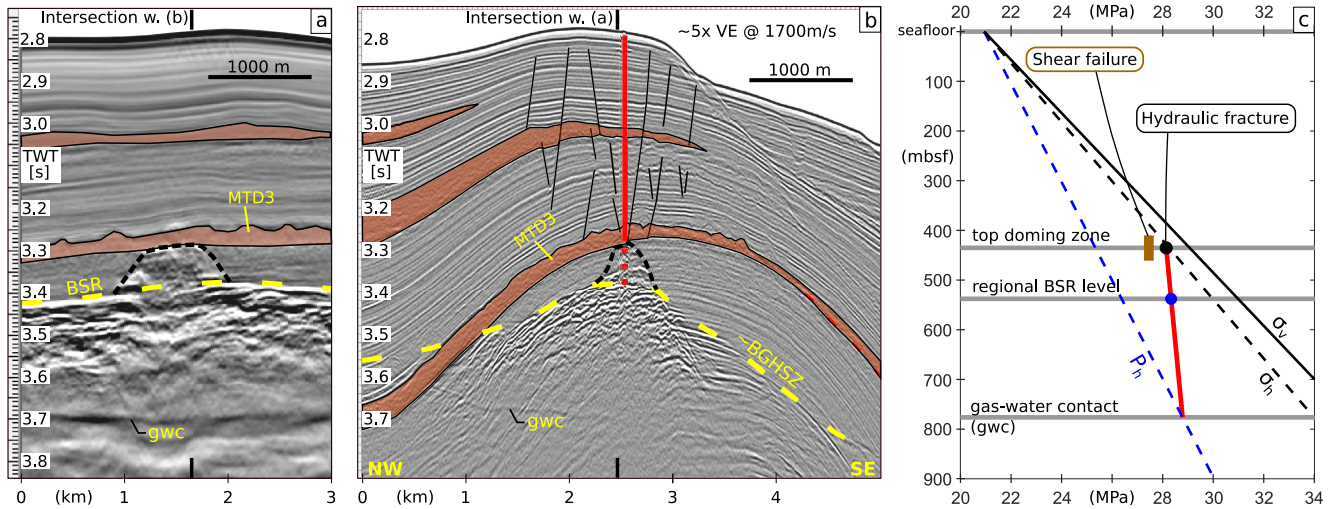


Figure 7. (a) Interpreted strike line (Line APB13-25, lower-frequency data, from Figure 2b). Labeled are: bottom simulating reflection (BSR) that marks the regional base of gas hydrate stability (BGHSZ); gas water contact (gwc) and Mass Transport Deposit 3 (MTD3). Bold broken black line outlines the high-amplitude doming zone, extending up from the BSR. Vertical exaggeration is $\sim 5\times$. (b) Interpreted dip line (Line TAN1808-97, higher-frequency data, from Figure 4b) plotted at same scale as the section in (a). Annotations as in (a). Vertical red line is the gas conduit, black lines are normal faults. (c) Estimated sub-seafloor stress state (see text for descriptions). P_h = hydrostatic fluid pressure; σ_h = horizontal stress; σ_v = vertical stress. Depths of top doming zone, regional BSR level and gas-water contact (gwc) are indicated. Red line shows effect of gas buoyancy pressure added to hydrostatic pressure. Blue dot = combined pressure at regional BSR level, black dot = combined pressure at top doming zone. Vertical brown tick at “top doming zone” = critical pressure for shear failure at this depth. The reader is referred to the Supporting Information S2 and S3 for assessments of uncertainty in depths of key horizons and the estimated horizontal stress (σ_h).

logging-while drilling data further north on the margin, as well as depth corrections of the “push down” effect at the gas-water contact.

In Figure 7c, we calculate sub-seafloor vertical stress σ_v according to Equation 1:

$$\sigma_v = \rho_b \cdot g \cdot z, \quad (1)$$

where ρ_b is bulk sediment density (kg/m^3), g is the gravitational acceleration constant (m/s^2) and z is depth (m) below seafloor. We use an average value of $1,910 \text{ kg}/\text{m}^3$ for ρ_b beneath the seafloor, based on mean bulk density of the upper 500 mbsf from three International Ocean Discovery Programme (IODP) drill sites (Sites U1517, U1518, and U1519) on the northern Hikurangi margin, some 450 km northeast of our study area (Pecher et al., 2018). Our plot of sub-seafloor vertical stress is added to hydrostatic pressure at the seafloor (20.9 MPa), which we calculate from the seafloor depth of 2,073 mbsl and a water density of $1,030 \text{ kg}/\text{m}^3$. The continuing hydrostatic pressure beneath the seafloor is also plotted in Figure 7c.

The vertical gas conduit and the normal fault network indicate that the ridge is undergoing extension, meaning the greatest principal stress is vertical (i.e., $\sigma_1 = \sigma_v$), and the least principal stress is horizontal (i.e., $\sigma_3 = \sigma_h$). The horizontal stress σ_h is the minimum pressure necessary for hydraulic fracturing.

We consider two approaches to estimate σ_h : (a) poro-elasticity under uniaxial strain and (b) the assumption that the system is undergoing coulomb failure along favorably oriented faults.

First, we use Poisson’s ratio ν to estimate σ_h , based on the assumption of linear elasticity and uniaxial strain (e.g., Daigle et al., 2020; Eaton, 1969) (Equation 2):

$$\sigma_h' = \frac{\nu}{1 - \nu} \sigma_v'. \quad (2)$$

σ_v' and σ_h' are the effective vertical and horizontal stresses, respectively—i.e., $\sigma_v' = \sigma_v - P_f$ and $\sigma_h' = \sigma_h - P_f$, where P_f is pore fluid pressure, which we here assume to be hydrostatic.

Poisson’s ratio (required in Equation 2) is determined from the relationship between P-wave velocity (V_p) and S-wave velocity (V_s) in Equation 3:

$$v = \frac{1 \left(\frac{V_p}{V_s} \right)^2 - 2}{2 \left(\frac{V_p}{V_s} \right)^2 - 1}, \quad (3)$$

where we take V_p from our velocity analysis (Figure 3a) and use Hamilton (1979) relationships for “silt clays, turbidites and mudstones” to estimate V_s at depth beneath the seafloor (Equation 4):

$$V_{s(z=0-36)} = 116 + 4.65 \cdot z; V_{s(z=36-120)} = 237 + 1.28 \cdot z; V_{s(z=120-650)} = 322 + 0.58 \cdot z, \quad (4)$$

where z is depth below seafloor in m and V_s is in m/s . Our estimate of Poisson's ratio at the top of the doming zone is 0.44, which is a reasonable value for shallow submarine sediments (Hamilton, 1979; Reynolds, 1997). The corresponding effective stress ratio $\frac{\sigma'_h}{\sigma'_v}$ of 0.78 is reasonable for this sub-seafloor depth (Dai et al., 2020) and would be typical of mudrocks that can act as effective sealing units (Casey et al., 2015).

Alternatively, we note that we could assume that the effective stress ratio is controlled by Coulomb failure along favorably oriented faults (e.g., Finkbeiner et al., 2001; Flemings, 2021). In this case the effective stress ratio is described by Equation 5:

$$\sigma'_h = \frac{1 - \sin\phi'}{1 + \sin\phi'} \sigma'_v \quad (5)$$

A friction angle (ϕ') of $\sim 8^\circ$ will produce a stress ratio of ~ 0.8 . While this friction angle is low it is not unreasonable for smectite rich mudrocks (Casey et al., 2015). In Supporting Information S3 we further explore the significant uncertainty in estimating σ'_h from σ'_v .

The gas-water capillary pressure (P_{cgw}) at the top of an interconnected free gas column is calculated with Equation 6:

$$P_{cgw} = (\rho_w - \rho_g) \cdot g \cdot z_1, \quad (6)$$

where ρ_w and ρ_g are the densities of water and methane gas, respectively (kg/m^3), and z_1 is the height (m) of the free gas reservoir (Flemings, 2021). This approach assumes that the capillary entry pressure for the reservoir is negligible. As above, we take the density of sea water to be $1,030 kg/m^3$. We estimate in-situ methane gas density to be $190 kg/m^3$, using Kossel et al. (2013) “SUGAR Toolbox”, based on ambient temperature and hydrostatic pressure at the depth of the BSR from the methane hydrate phase boundary (Tishchenko et al., 2005). In Figure 7c, we add the gas-water capillary pressure P_{cgw} to hydrostatic pressure to show gas phase pressure (red line) under the assumption of hydrostatic pore water pressure, and compare it to the estimated in-situ stress conditions. The black dot in Figure 7c shows that our estimate of gas phase pressure approximately equals the estimated fracture gradient σ'_h at the top of the doming zone. This indicates that hydraulic fracturing is feasible at the top of the doming zone, i.e., the base of MTD3, under hydrostatic pore water pressure conditions. In contrast, hydraulic fracturing at the depth of the regional BSR would not be feasible under hydrostatic pressure conditions (blue dot is well below σ'_h at that depth). In Supporting Information S3 we evaluate how uncertainties in both sub-seafloor depths and the effective stress ratio propagate into uncertainties in the relationship between gas phase pressure and σ'_h . This uncertainty analysis underscores the feasibility of hydraulic fracturing at the top of the doming zone under hydrostatic pore water pressure conditions. It also shows that hydraulic fracturing at the regional BSR level is unlikely under hydrostatic pore water pressure, even for the least mechanically stable case in our uncertainty analysis.

Based on Figure 7c, and the uncertainty analysis in Supporting Information S3, we present our interpretation of the development of the vertical gas conduit in the conceptual sketches of Figure 8. The geometry of Figure 8 is based on the section in Figure 7b, with depth conversion based on representative sub-seafloor velocities from Figure 3a. The thick (up to 240 m) free gas column that has accumulated beneath the regional BGHSZ implies that the BGHSZ has acted as a significant capillary seal. The capillary seal presumably formed as a result of hydrates filling the largest pores (e.g., Fang et al., 2020). We assume that inherent lithological permeability barriers (i.e., impeding flow across the folded layers) also played a role in trapping the free gas at the regional BGHSZ level, since strata are sub-parallel to the BGHSZ. Once the gas column reached the thickness required for capillary entry at the BGHSZ level, free gas migrated upward and intercepted MTD3 (Stage 1; Figure 8b). Some degree of subsequent free gas trapping and lateral flow at the base of MTD3 is implied by the free gas accumulations at that depth, directly beneath MTD3 (e.g.,

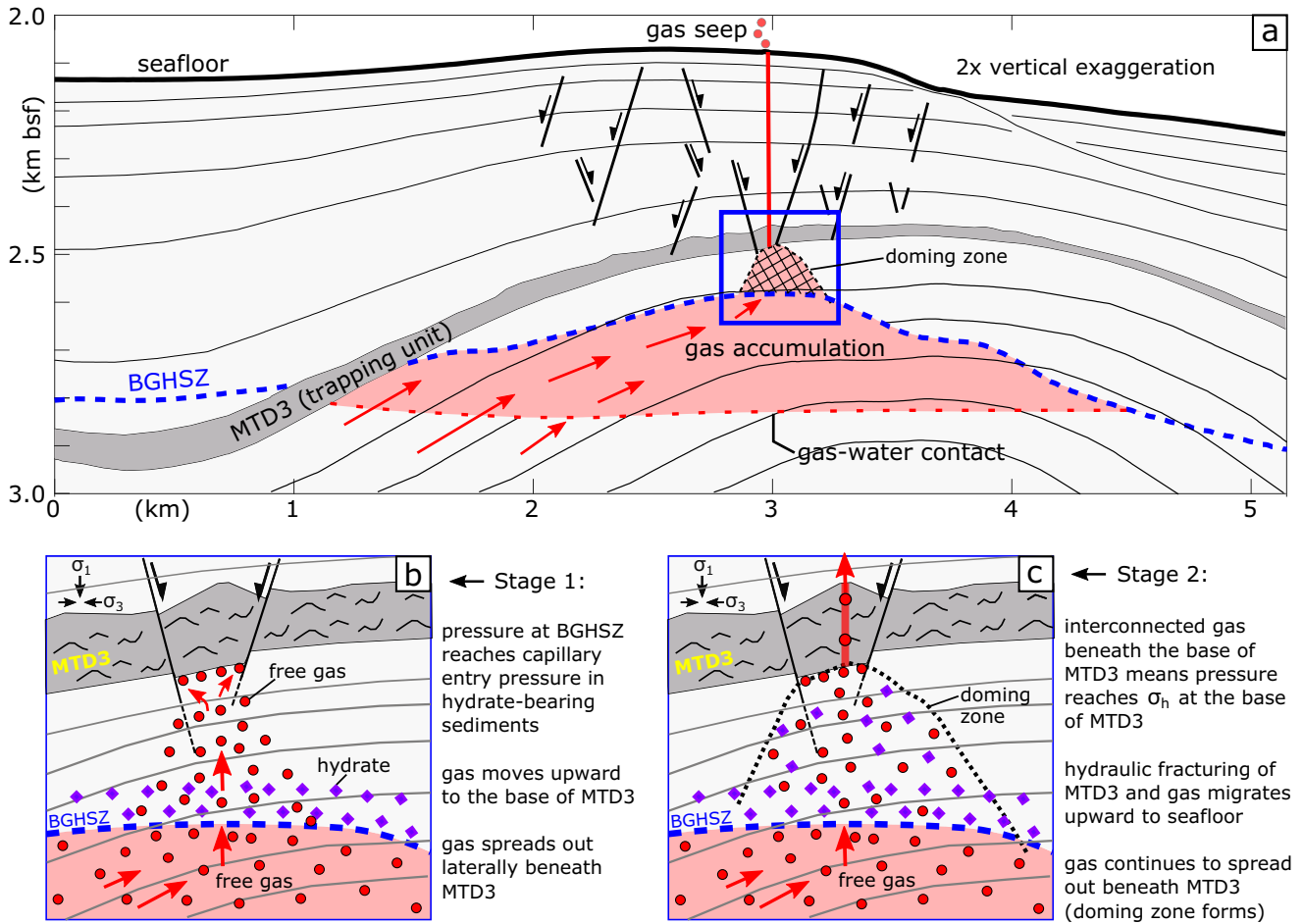


Figure 8. Sketch of interpreted gas migration scenario beneath the ridge. (a) Large-scale section, based on the geometry in Figure 7b, with depth conversion based on velocities from Figure 3a. Interpreted flow paths (red arrows) shown beneath the base of the gas hydrate stability zone (BGHSZ; broken blue line). MTD3 = Mass Transport Deposit 3. Cross-hatched region doming up from the BGHSZ beneath the center of the ridge = doming zone. (b) Enlargement from region in blue box in (a), around the doming zone, depicting our interpretation of Stage 1 of gas conduit development. BGHSZ is the broken blue line. Free gas depicted by red circles; hydrate by purple diamonds. (c) Same field of view as (b), showing our interpretation of Stage 2, and the development of the doming zone (within the dotted black line).

Figures 4a, 4b, 5a, and 5b). With free gas then interconnected between the gas-water contact and the base of MTD3, the gas phase pressure reached the fracture gradient (σ_h) in MTD3 and hydraulic fracturing propagated through to the seafloor (Stage 2; Figure 8c). Gas continued to spread out beneath MTD3, forming the high-amplitude doming zone of mixed gas and gas hydrate between the regional BGHSZ level and the base of MTD3. Finally, we interpret that the entire system at the present day is in a gas-rich state of equilibrium; as more gas is added to the reservoir it “bleeds off” out of the top, through the gas conduit to the seafloor. In the absence of any drilling data (e.g., bulk density data), we cannot make any reliable estimate of gas saturation within the reservoir. However, as a comparison, we note that gas saturations exceeding 60% have been inferred in the free gas column within “Horizon A” beneath Hydrate Ridge on the Cascadia Margin (Tréhu, Flemings, et al., 2004).

While Figure 8 depicts our preferred interpretation for this system, we note that it is also possible that hydraulic fracturing initiated at the deeper regional BGHSZ level rather than at the base of MTD3. This alternative scenario would require either supra-hydrostatic water pressure (Flemings et al., 2003) or a significantly lower effective stress ratio $\frac{\sigma_h}{\sigma_v}$ in the reservoir sediments at the BGHSZ level, or a combination of both. Our sensitivity testing (Figure S4) suggests that excess water pressure would likely be required even in the case of a lower bound effective stress ratio (0.5) in the reservoir sediments.

4.5. Normal Faults: Often Ignored as Gas Flow Conduits?

Uplifted ridges in accretionary wedges are commonly associated with shallow normal fault systems that accommodate gravitational collapse of the local relief that is caused by the geometry of folding (e.g., Morley, 2009; Weinberger & Brown, 2006). Although there are examples elsewhere of normal faults acting as preferred free gas migration pathways through the GHSZ (e.g., Böttner et al., 2018), it is interesting that normal faults are often not utilized and free gas migration through the GHSZ succeeds by establishing a conduit through “new” hydraulic fracturing systems (e.g., Riedel et al., 2018). At the ridge in this study, the vertical conduit has formed amid an array of normal faults (Figures 4a and 4b). For reference, we have plotted the critical pressure (P_{shear}) required for shear failure at the top of the doming zone in Figure 7c, which is lower than the pressure required for hydraulic fracturing. This approach to predict P_{shear} was described by Finkbeiner et al. (2001) and is given by Equation 7 (Flemings, 2021):

$$P_{\text{shear}} = \frac{\sigma_h - \left(\frac{1 - \sin\phi'}{1 + \sin\phi'} \right) \sigma_v}{\left[1 - \left(\frac{1 - \sin\phi'}{1 + \sin\phi'} \right) \right]}, \quad (7)$$

where ϕ' is the friction angle of the reactivated normal faults, which can be estimated from Equation 8, from the dip angle of the faults (θ), which we estimate as 60° .

$$\phi' = \text{abs}(90 - 2\theta). \quad (8)$$

Although there is tentative evidence for upward free gas migration along a short segment of a single fault (i.e., up to ~ 130 m vertically; Figure 2a-inset), the migration of free gas through to shallower depths succeeds solely through the vertical conduit. A similar general observation has been made from 3D seismic data at Opouawe Bank, ~ 20 km NE from here (Figure 1b), where elongated vertical fluid conduits enable gas seepage at the seafloor, despite widespread normal faulting throughout the GHSZ (Riedel et al., 2018).

In general, faults that are conductive to fluid flow are those that are critically stressed for shear failure (Barton et al., 1995; Townend & Zoback, 2000). Importantly though, in a comprehensive study of natural CO_2 leakage on the Colorado Plateau, Naruk et al. (2019) observed that the faults that leak are those where (1) there is a fractured fault damage zone and (2) the total fluid pressure reduces the horizontal effective stress to approximately zero. Criterion (2) must have been met at the base of the gas conduit in this study, since the vertical conduit has formed by fluid pressure exceeding the horizontal effective stress. On the other hand, it is unknown whether criterion (1) is met within the normal faults that extend to these depths (e.g., those in Figures 5a and 5b). In some cases, shearing can thwart hydraulic conductivity due to a reduction of matrix porosity and permeability, or through the formation of ductile smears in the case of diagenetically immature shales (Naruk et al., 2019; Zoback, 2010). Also of relevance in shallow gas hydrate-bearing sediments is the likelihood that the entire sediment column between the seafloor and the BGHSZ is relatively incompetent (soft sediments). Such strata will presumably have a low tendency to accommodate dilatational strain along fault segments during sliding because of soft sediment deformation. We suggest that one or more of these factors could explain an apparent lack of leaking normal faults in the GHSZ on the southern Hikurangi margin.

4.6. Other Examples of Doming Zones Beneath Gas Conduits?

Our observation of a distinct doming zone beneath a gas conduit, and directly above the regional BSR level, has implications for understanding gas hydrate formation around gas conduits. Zones of mixed free gas and gas hydrate are known to form in nature close to the seafloor around gas conduits (Haeckel et al., 2004; Tréhu, Flemings, et al., 2004; Tréhu, Long, et al., 2004), manifesting themselves as disrupted but strong reflectivity in seismic data (e.g., Crutchley et al., 2013; Riedel et al., 2018; Tréhu, Long, et al., 2004). Our results in this study indicate that broad zones of free gas and gas hydrate can also develop at the bases of gas conduits, in agreement with previous numerical modeling studies (e.g., Chatterjee et al., 2014; Liu et al., 2019). There are other examples in nature of doming reflectivity above the regional BSR level at the bases of gas conduits (e.g., Koch et al., 2016). However, there are also many examples where this doming phenomenon does not occur (e.g., Petersen et al., 2010; Plaza-Faverola et al., 2011), including in cases where

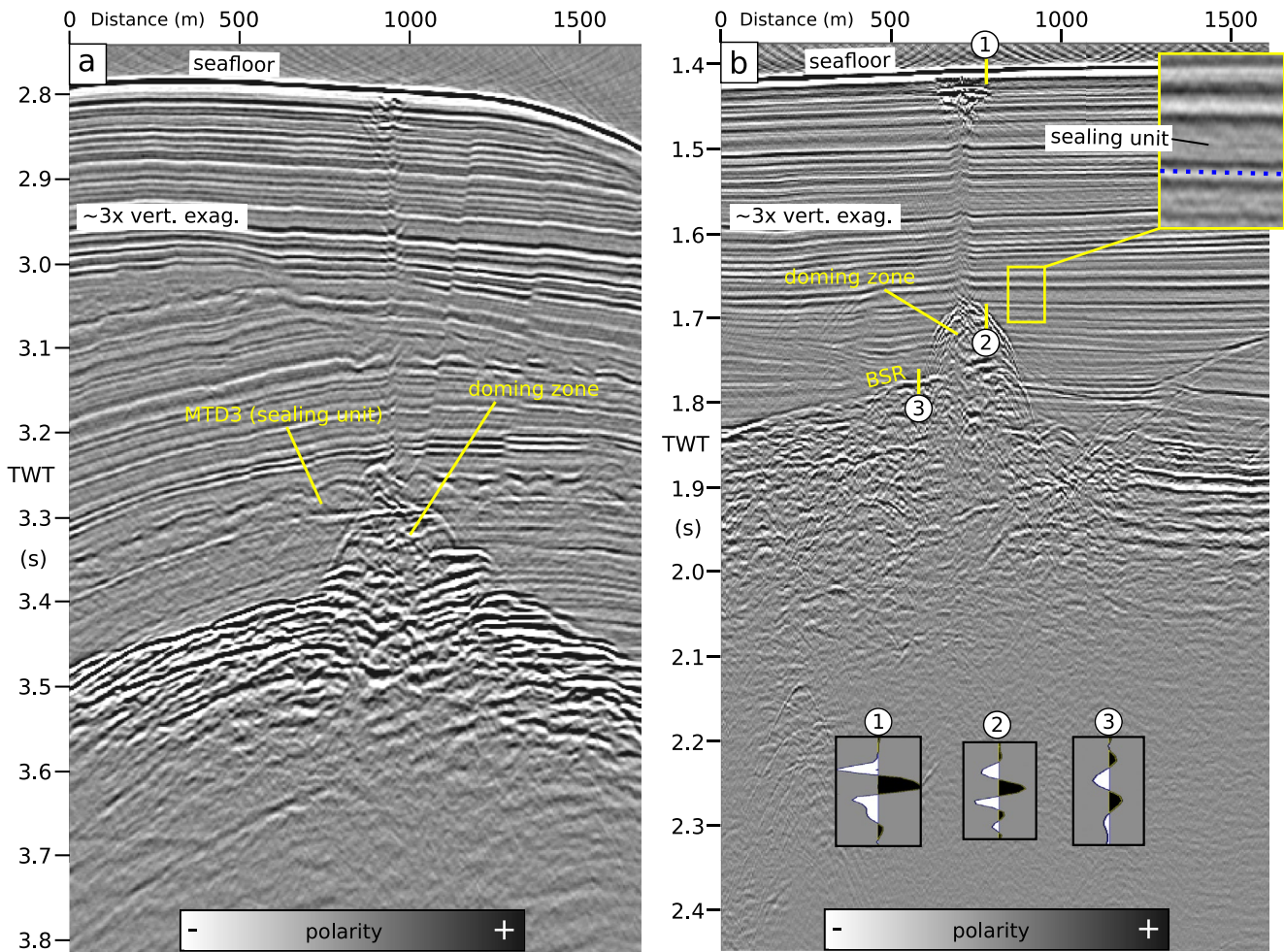


Figure 9. Comparison between gas conduits, plotted at identical horizontal and vertical scales. The vertical exaggeration is $\sim 3x$, based on a representative sediment velocity of 1,600 m/s. TWT = two-way travel time. (a) The conduit in this study, from Line TAN1808-92 (Figure 4a), with the doming zone annotated. (b) A gas conduit beneath the Takahē Seep (see Figure 1b for location). Example waveforms show polarity at the seafloor (position “1”), at an example location at the top of the doming zone (position “2”), and at the bottom simulating reflection (BSR) (position “3”). Yellow box enlargement (upper right) shows the sealing unit at the top of the doming zone, the base of which is marked by a negative polarity reflection (dotted blue line).

high seismic velocities point to concentrated gas hydrate accumulations within and around gas conduits (Plaza-Faverola et al., 2010).

In Figure 9 we compare the gas conduit in this study with another example gas conduit, beneath the Takahē seep site (Koch et al., 2016) (~ 20 km to the northeast, see Figure 1). The two doming zones have similar dimensions, despite having formed in different water depths. There is also evidence from waveform polarity (Figure 9b) for gas hydrate in the doming zone surrounding the base of the Takahē conduit. The doming zone at Takahē is capped by a regional negative polarity reflection that marks the base of a weakly reflective unit, which has acted as the seal (Figure 9b). From these two examples, it appears likely that the causes of such doming zones are compacted lithological units above the BGHSZ, which divert some of the ascending free gas laterally. The sealing units in both examples are ~ 100 ms (or ~ 80 – 100 m) above the regional BGHSZ level. The sealing unit in Figure 9a is the mass transport deposit (MTD3), while it is unclear what the lithological origin of the sealing unit is in Figure 9b.

Since vertical gas conduits influence seafloor ecology and ocean chemistry (e.g., Levin et al., 2016) as well as subsurface gas hydrate formation (e.g., Haeckel et al., 2004; Tréhu, Flemings, et al., 2004), it is important to explore how geological settings control their development. This study has demonstrated the important role of lithological seals (in this case a folded mass transport deposit; Figure 8) in constraining the lateral and

vertical distribution of a thick free gas reservoir. Such seals can also lead to doming zones of free gas and gas hydrate extending upward from the regional BGHSZ around gas conduits. We suggest that future modeling of gas conduit propagation might consider the role of pronounced lithological contrasts within the hydrate stability zone, and how such heterogeneity influences free gas flow and gas hydrate formation.

5. Conclusions

We have presented seismic reflection images of a classic gas conduit through the GHSZ, amid a network of normal faults. We draw the following conclusions about the gas hydrate/free gas system:

1. The gas conduit is underlain by a thick free gas zone, the base of which is marked by a distinct reflection from the gas-water contact that cuts across dipping lithological reflectors. At its thickest point, the free gas zone is ~240 m thick, from the BSR to the gas-water contact.
2. The interconnected free gas column has led to capillary entry into the GHSZ and, ultimately, to hydraulic fracturing of the overburden and propagation of the gas conduit through to the seafloor. Though there is evidence for relatively short free gas migration along a single fault, the broader normal fault network is not exploited for large-scale free gas migration through the hydrate stability zone.
3. Beneath the gas conduit is an upward doming zone of higher-than-background reflectivity. This doming zone extends upward from the regional base of hydrate stability (as determined from BSRs in low-frequency data) and contains both positive- and negative-polarity reflections. Note that the term “doming” in this context refers to the shape of enhanced reflectivity, and does not refer to physical doming of stratigraphic layers.
4. We interpret the doming zone as a region of free gas and gas hydrate that formed directly beneath the gas conduit, prior to the gas conduit developing. Lateral spread of fluid beneath the gas conduit has likely been encouraged by a sealing mass transport deposit.
5. Doming zones like the one described in this study have also been observed beneath other gas conduits, but they are not inherent to all gas conduits through hydrate-bearing sediments globally. We suggest that they form in places where there are pronounced lithological seals within the hydrate stability zone that trap some of the ascending free gas and deflect it laterally.

Conflict of Interest

The authors declare no conflicts of interest relevant to this study.

Data Availability Statement

Data presented in this paper are available at the following online repository: <https://doi.pangaea.de/10.1594/PANGAEA.925897>, together with information for viewing the data.

References

- Amundsen, L., Reichel, T., & Landro, M. (2015). Gas Hydrates - Part V: The Resource Potential. *GEOExPro magazine*, 11(6). Retrieved from <https://www.geoexpro.com/articles/2015/02/gas-hydrates-part-v-the-resource-potential>
- Anadarko New Zealand Ltd. (2014). *Seismic Data Processing Report - APB-13-2D Pegasus Basin 2D PEP54858*. NZP&M, Ministry of Business, Innovation & Employment (MBIE), New Zealand Unpublished Petroleum Report PR5171.
- Ballance, P. F. (1976). Evolution of the upper cenozoic magmatic arc and plate boundary in northern New Zealand. *Earth and Planetary Science Letters*, 28(3), 356–370. [https://doi.org/10.1016/0012-821x\(76\)90197-7](https://doi.org/10.1016/0012-821x(76)90197-7)
- Barnes, P. M., de Lépinay, B. M., Collot, J.-Y., Delteil, J., & Audru, J.-C. (1998). Strain partitioning in the transition area between oblique subduction and continental collision. *Hikurangi margin, New Zealand: Tectonics*, 17(4), 534–557. <https://doi.org/10.1029/98tc00974>
- Barnes, P. M., Lamarche, G., Bialas, J., Henrys, S., Pecher, L., Netzeband, G. L., et al. (2010). Tectonic and geological framework for gas hydrates and cold seeps on the Hikurangi subduction margin, New Zealand. *Marine Geology*, 272(1–4), 26–48. <https://doi.org/10.1016/j.margeo.2009.03.012>
- Barton, C. A., Zoback, M. D., & Moos, D. (1995). Fluid flow along potentially active faults in crystalline rock. *Geology*, 23(8), 683–686.
- Berndt, C., Chi, W. C., Jegen, M., Lebas, E., Crutchley, G., Muff, S., et al. (2019). Tectonic controls on gas hydrate distribution off SW Taiwan. *Journal of Geophysical Research: Solid Earth*, 124, 1164–1184.
- Biaostoch, A., Treude, T., Rüpke, L. H., Riebesell, U., Roth, C., Burwicz, E. B., et al. (2011). Rising Arctic Ocean temperatures cause gas hydrate destabilization and ocean acidification. *Geophysical Research Letters*, 38, 1–5. <https://doi.org/10.1029/2011gl047222>
- Boswell, R., Collett, T. S., Frye, M., Shedd, W., McConnell, D. R., & Shelander, D. (2012). Subsurface gas hydrates in the northern Gulf of Mexico. *Marine and Petroleum Geology*, 34(1), 4–30. <https://doi.org/10.1016/j.marpetgeo.2011.10.003>

Acknowledgments

Funding for this research was provided by New Zealand's Ministry for Business, Innovation and Employment, contract C05X1708. The authors thank the captain (Doug Monks) and the crew of *RV Tangaroa* for their excellent assistance during collection of seismic data and multibeam water column and bathymetry data, during Voyage TAN1808. The authors are very grateful for thorough reviews from Seth Haines and Associate Editor Anne Bécel, which led to a significant improvement of this paper from the first submitted version. The authors also thank Karsten Kroeger, Mac Beggs and Ray Boswell for stimulating discussions about this work, and the Editor Douglas Schmitt for handling of this submission. Seismic processing was carried out using an academic license to GLOBE Claritas. Seismic interpretation used an academic license to the Kingdom Suite software. Open access funding enabled and organized by Projekt DEAL.

- Böttner, C., Gross, F., Geersen, J., Crutchley, G. J., Mountjoy, J. J., & Krastel, S. (2018). Marine forearc extension in the Hikurangi margin: New insights from high-resolution 3-D seismic data. *Tectonics*, 37(5), 1472–1491. <https://doi.org/10.1029/2017tc004906>
- Brooks, J. M., Anderson, A. L., Sassen, R., Kennicutt, M. C., & Guinasso, N. L., Jr (1994). Hydrate occurrences in shallow subsurface cores from continental slope sediments. *Annals of the New York Academy of Sciences*, 715(1), 381–391. <https://doi.org/10.1111/j.1749-6632.1994.tb38851.x>
- Brown, A. R., & Abriel, W. L. (2014). The polarity of zero-phase wavelets. *Interpretation*, 2(1). <https://doi.org/10.1190/INT2013-1202-PS.1>
- Casey, B., Germaine, J. T., Flemings, P. B., & Fahy, B. P. (2015). Estimating horizontal stresses for mudrocks under one-dimensional compression. *Marine and Petroleum Geology*, 65, 178–186. <https://doi.org/10.1016/j.marpetgeo.2015.02.001>
- Chadwick, R. A., Williams, G. A., & Falcon-Suarez, I. (2019). Forensic mapping of seismic velocity heterogeneity in a CO₂ layer at the Sleipner CO₂ storage operation, North Sea, using time-lapse seismics. *International Journal of Greenhouse Gas Control*, 90, 102793. <https://doi.org/10.1016/j.ijggc.2019.102793>
- Chatterjee, S., Bhatnagar, G., Dugan, B., Dickens, G. R., Chapman, W. G., & Hirasaki, G. J. (2014). The impact of lithologic heterogeneity and focused fluid flow upon gas hydrate distribution in marine sediments. *Journal of Geophysical Research: Solid Earth*, 119, 6705–6732. <https://doi.org/10.1002/2014JB011236>
- Clennell, M. B., Hovland, M., Booth, J. S., Henry, P., & Winters, W. J. (1999). Formation of natural gas hydrates in marine sediments: 1. Conceptual model of gas hydrate growth conditioned by host sediment properties. *Journal of Geophysical Research*, 104(B10), 22985–23003. <https://doi.org/10.1029/1999jb900175>
- Crutchley, G. J., Berndt, C., Geiger, S., Klaeschen, D., Papenberg, C., Klaucke, I., et al. (2013). Drivers of focused fluid flow and methane seepage at south Hydrate Ridge, offshore Oregon, USA. *Geology*, 41(5), 551–554. <https://doi.org/10.1130/g34057.1>
- Crutchley, G. J., Kroeger, K. F., Pecher, I. A., & Gorman, A. R. (2018). How tectonic folding influences gas hydrate formation: New Zealand's Hikurangi subduction margin. *Geology*, 47(1), 39–42. <https://doi.org/10.1130/g45151.1>
- Crutchley, G. J., Mountjoy, J. J., Davy, B. D., Hillman, J. I. T., Watson, S., Stewart, L., et al. (2018). *Gas Hydrate Systems of the Southern Hikurangi Margin, Aotearoa, New Zealand. TAN1808 Voyage Report, RV Tangaroa 8-Sep – 5 Oct 2018. Lower Hutt (NZ): GNS Science. 83p.* GNS Science report. <https://doi.org/10.21420/73WW-1W83>
- Daigle, H., Cook, A., Fang, Y., Bihani, A., Song, W., & Flemings, P. B. (2020). Gas-driven tensile fracturing in shallow marine sediments. *Journal of Geophysical Research: Solid Earth*, 125, e2020JB020835. <https://doi.org/10.1029/2020JB020835>
- Day-Stirrat, R. J., Flemings, P. B., You, Y., & van der Pluijm, B. A. (2013). Modification of mudstone fabric and pore structure as a result of slope failure: Ursa Basin, Gulf of Mexico. *Marine Geology*, 341, 58–67. <https://doi.org/10.1016/j.marpetgeo.2013.05.003>
- DeMets, C., Gordon, R. G., & Argus, D. F. (2010). Geologically current plate motions. *Geophysical Journal International*, 181(1), 1–80. <https://doi.org/10.1111/j.1365-246x.2009.04491.x>
- Dix, C. H. (1955). Seismic velocities from surface measurements. *Geophysics*, 20(1), 68–86. <https://doi.org/10.1190/1.1438126>
- Dugan, B. (2012). Petrophysical and consolidation behavior of mass transport deposits from the northern Gulf of Mexico, IODP Expedition 308. *Marine Geology*, 315, 98–107. <https://doi.org/10.1016/j.marpetgeo.2012.05.001>
- Eaton, B. A. (1969). Fracture gradient prediction and its application in oilfield operations. *Journal of Petroleum Technology*, 21(10), 353–351. <https://doi.org/10.2118/2163-pa>
- Fang, Y., Flemings, P. B., Daigle, H., Phillips, S. C., Meazell, P. K., & You, K. (2020). Petrophysical properties of the Green Canyon Block 955 hydrate reservoir inferred from reconstituted sediments: Implications for hydrate formation and production. *AAPG Bulletin*, 104(9), 1997–2028. <https://doi.org/10.1306/01062019165>
- Finkbeiner, T., Zoback, M., Flemings, P., & Stump, B. (2001). Stress, pore pressure, and dynamically constrained hydrocarbon columns in the South Eugene Island 330 Field, Northern Gulf of Mexico. *AAPG Bulletin*, 85(6), 1007–1031. <https://doi.org/10.1306/8626ca55-173b-11d7-8645000102c1865d>
- Flemings, P. B. (2021). *A concise guide to geopressure: Origin, prediction, and applications*. Cambridge University Press.
- Flemings, P. B., Liu, X., & Winters, W. J. (2003). Critical pressure and multiphase flow in Blake Ridge gas hydrates. *Geology*, 31(12), 1057–1060. <https://doi.org/10.1130/g19863.1>
- Fraser, D. R., Gorman, A. R., Pecher, I. A., Crutchley, G. J., & Henry, S. A. (2016). Gas hydrate accumulations related to focused fluid flow in the Pegasus Basin, southern Hikurangi Margin, New Zealand. *Marine and Petroleum Geology*, 77, 399–408. <https://doi.org/10.1016/j.marpetgeo.2016.06.025>
- Fu, X., Jimenez-Martinez, J., Nguyen, T. P., Carey, J. W., Viswanathan, H., Cueto-Felgueroso, L., & Juanes, R. (2020). Crustal fingering facilitates free-gas methane migration through the hydrate stability zone. *Proceedings of the National Academy of Sciences*, 117(50), 31660–31664. <https://doi.org/10.1073/pnas.2011064117>
- Gorman, A. R., Holbrook, W. S., Hornbach, M. J., Hackwith, K. L., Lizarralde, D., & Pecher, I. (2002). Migration of methane gas through the hydrate stability zone in a low-flux hydrate province. *Geology*, 30(4), 327–330. [https://doi.org/10.1130/0091-7613\(2002\)030<0327:MOMGTT>2.0.CO;2](https://doi.org/10.1130/0091-7613(2002)030<0327:MOMGTT>2.0.CO;2)
- Greiner, J., Lewis, K. B., Bialas, J., Pecher, I., Rowden, A. A., Bowden, D., et al. (2010). Methane seepage along the Hikurangi Margin, New Zealand: Overview of studies in 2006 and 2007 and new evidence from visual, bathymetric and hydroacoustic investigations. *Marine Geology*, 272, 6–25. <https://doi.org/10.1016/j.marpetgeo.2010.01.017>
- Haackel, M., Suess, E., Wallmann, K., & Rickert, D. (2004). Rising methane gas bubbles form massive hydrate layers at the seafloor. *Geochimica et Cosmochimica Acta*, 68(21), 4335–4345. <https://doi.org/10.1016/j.gca.2004.01.018>
- Haines, S. S., Hart, P. E., Collett, T. S., Shedd, W., Frye, M., Weimer, P., & Boswell, R. (2017). High-resolution seismic characterization of the gas and gas hydrate system at Green Canyon 955, Gulf of Mexico, USA. *Marine and Petroleum Geology*, 82, 220–237. <https://doi.org/10.1016/j.marpetgeo.2017.01.029>
- Hamilton, E. L. (1979). V_p/V_s and Poisson's ratios in marine sediments and rocks. *Journal of the Acoustical Society of America*, 66(4), 1093–1101. <https://doi.org/10.1121/1.383344>
- Hornbach, M. J., Saffer, D. M., & Holbrook, W. S. (2004). Critically pressured free-gas reservoirs below gas-hydrate provinces. *Nature*, 427, 142–144. <https://doi.org/10.1038/nature02172>
- Katz, H. R. (1982). Evidence of gas hydrates beneath the continental slope, East Coast, North Island, New Zealand. *Journal of Geology and Geophysics*, 25(2), 193–199. <https://doi.org/10.1080/00288306.1982.10421408>
- Koch, S., Schroeder, H., Haackel, M., Berndt, C., Bialas, J., Papenberg, C., et al. (2016). Gas migration through Opouawe Bank at the Hikurangi margin offshore New Zealand. *Geo-Marine Letters*, 36(3), 187–196. <https://doi.org/10.1007/s00367-016-0441-y>
- Kossel, E., Bigalke, N. K., Piner, E., & Haackel, M. (2013). *The SUGAR Toolbox: A library of numerical algorithms and data for modelling of gas hydrate systems and marine environments*.

- Kroeger, K. F., Crutchley, G. J., Kellett, R., & Barnes, P. M. (2019). A 3-D model of gas generation, migration, and gas hydrate formation at a young convergent margin (Hikurangi margin, New Zealand). *Geochemistry, Geophysics, Geosystems*, 20(11), 5126–5147. <https://doi.org/10.1029/2019gc008275>
- Kroeger, K. F., Plaza-Faverola, A., Barnes, P. M., & Pecher, I. A. (2015). Thermal evolution of the New Zealand Hikurangi subduction margin: Impact on natural gas generation and methane hydrate formation—A model study. *Marine and Petroleum Geology*, 63, 97–114. <https://doi.org/10.1016/j.marpetgeo.2015.01.020>
- Levin, L. A., Baco, A. R., Bowden, D. A., Colaco, A., Cordes, E. E., Cunha, M. R., et al. (2016). Hydrothermal vents and methane seeps: Rethinking the Sphere of Influence. *Frontiers in Marine Science*, 3–72. <https://doi.org/10.3389/fmars.2016.00072>
- Liu, J., Haeckel, M., Rutqvist, J., Wang, S., & Yan, W. (2019). The mechanism of methane gas migration through the gas hydrate stability zone: Insights from numerical simulations. *Journal of Geophysical Research: Solid Earth*, 124, 4399–4427. <https://doi.org/10.1029/2019jb017417>
- Liu, X., & Flemings, P. B. (2006). Passing gas through the hydrate stability zone at southern Hydrate Ridge, offshore Oregon. *Earth and Planetary Science Letters*, 241(1–2), 211–226. <https://doi.org/10.1016/j.epsl.2005.10.026>
- MacDonald, I. R., Sager, W. W., & Peccini, M. B. (2003). Gas hydrate and chemosynthetic biota in mounded bathymetry at mid-slope hydrocarbon seeps: Northern Gulf of Mexico. *Marine Geology*, 198(1), 133–158. [https://doi.org/10.1016/s0025-3227\(03\)00098-7](https://doi.org/10.1016/s0025-3227(03)00098-7)
- Morley, C. (2009). Geometry of an oblique thrust fault zone in a deepwater fold belt from 3D seismic data. *Journal of Structural Geology*, 31(12), 1540–1555. <https://doi.org/10.1016/j.jsg.2009.08.015>
- Naruk, S., Solum, J., Brandenburg, J., Origo, P., & Wolf, D. (2019). Effective stress constraints on vertical flow in fault zones: Learnings from natural CO₂ reservoirs. *AAPG Bulletin*, 103(8), 1979–2008. <https://doi.org/10.1306/12181817393>
- Pecher, I. A., Barnes, P. M., LeVay, L. J., & the Expedition 372 Scientists. (2018). Expedition 372 Preliminary Report: Creeping gas hydrate slides and Hikurangi LWD. *International Ocean Discovery Program*. <https://doi.org/10.14379/iodp.pr.372.2018>
- Pecher, I. A., & Henrys, S. A. (2003). *Potential gas reserves in gas hydrate sweet spots on the Hikurangi Margin* (p. 32). New Zealand: Lower Hutt, New Zealand, Institute of Geological and Nuclear Sciences Science Report.
- Petersen, C. J., Büinz, S., Hustoft, S., Mienert, J., & Klaeschen, D. (2010). High-resolution P-Cable 3D seismic imaging of gas chimney structures in gas hydrated sediments of an Arctic sediment drift. *Marine and Petroleum Geology*, 27. <https://doi.org/10.1016/j.marpetgeo.2010.06.006>
- Plaza-Faverola, A., Büinz, S., & Mienert, J. (2011). Repeated fluid expulsion through sub-seabed chimneys offshore Norway in response to glacial cycles. *Earth and Planetary Science Letters*, 1–12. <https://doi.org/10.1016/j.epsl.2011.03.001>
- Plaza-Faverola, A., Klaeschen, D., Barnes, P., Pecher, I., Henrys, S., & Mountjoy, J. (2012). Evolution of fluid expulsion and concentrated hydrate zones across the southern Hikurangi subduction margin, New Zealand: An analysis from depth migrated seismic data. *Geochemistry, Geophysics, Geosystems*, 13(8).
- Plaza-Faverola, A., Westbrook, G. K., Ker, S., Exley, R. J., Gailler, A., Minshull, T. A., & Broto, K. (2010). Evidence from three-dimensional seismic tomography for a substantial accumulation of gas hydrate in a fluid-escape chimney in the Nyegga pockmark field, offshore Norway. *Journal of Geophysical Research*, 115.
- Reynolds, J. M. (1997). *An introduction to applied and environmental geophysics*. Chichester, UK: John Wiley.
- Riedel, M., Crutchley, G., Koch, S., Berndt, C., Bialas, J., Eisenberg-Klein, G., et al. (2018). *Elongate fluid flow structures: Stress control on gas migration at Opouawe Bank, New Zealand*. Marine and Petroleum Geology.
- Rocha-Legorreta, F. J. (2009). Seismic evidence and geological distinctiveness related to gas hydrates in Mexico. *The Leading Edge*, 28, 714–717. <https://doi.org/10.1190/L3148414>
- Sawyer, D. E., Flemings, P. B., Dugan, B., & Germaine, J. T. (2009). Retrogressive failures recorded in mass transport deposits in the Ursa Basin, Northern Gulf of Mexico. *Journal of Geophysical Research*, 114. <https://doi.org/10.1029/2008jb006159>
- Schwalenberg, K., Haeckel, M., Poort, J., & Jegen, M. (2010). Evaluation of gas hydrate deposits in an active seep area using marine controlled source electromagnetics: Results from Opouawe Bank, Hikurangi Margin, New Zealand. *Marine Geology*, 272(1–4), 79–88. <https://doi.org/10.1016/j.marpetgeo.2009.07.006>
- Singh, S. C., Minshull, T. A., & Spence, G. D. (1993). Velocity structure of a gas hydrate reflector. *Science*, 260(5105), 204–207. <https://doi.org/10.1126/science.260.5105.204>
- Stern, T. A., Stratford, W. R., & Salmon, M. L. (2006). Subduction evolution and mantle dynamics at a continental margin: Central North Island, New Zealand. *Reviews of Geophysics*, 44(4). <https://doi.org/10.1029/2005rg000171>
- Sun, Q., Alves, T., Xie, X., He, J., Li, W., & Ni, X. (2017). Free gas accumulations in basal shear zones of mass-transport deposits (Pearl River Mouth Basin, South China Sea): An important geohazard on continental slope basins. *Marine and Petroleum Geology*, 81, 17–32. <https://doi.org/10.1016/j.marpetgeo.2016.12.029>
- Tishchenko, P., Hensen, C., Wallmann, K., & Wong, C. S. (2005). Calculation of the stability and solubility of methane hydrate in seawater. *Chemical Geology*, 219, 37–52. <https://doi.org/10.1016/j.chemgeo.2005.02.008>
- Townend, J., & Zoback, M. D. (2000). How faulting keeps the crust strong. *Geology*, 28(5), 399–402. [https://doi.org/10.1130/0091-7613\(2000\)028<0399:HFKTCS>2.3.CO;2](https://doi.org/10.1130/0091-7613(2000)028<0399:HFKTCS>2.3.CO;2)
- Tréhu, A. M., Flemings, P. B., Bangs, N. L., Chevallier, J., Grácia, E., Johnson, J. E., et al. (2004). Feeding methane vents and gas hydrate deposits at south Hydrate Ridge. *Geophysical Research Letters*, 31, 1–4. <https://doi.org/10.1029/2004gl021286>
- Tréhu, A. M., Long, P. E., Torres, M. E., Bohrmann, G. R. R. F., Rack, F. R., Collett, T. S., et al. (2004). Three-dimensional distribution of gas hydrate beneath southern Hydrate Ridge: Constraints from ODP Leg 204. *Earth and Planetary Science Letters*, 222(3–4), 845–862. <https://doi.org/10.1016/j.epsl.2004.03.035>
- Vanneste, M., De Batist, M., Golmshtok, A., Kremlev, A., & Versteeg, W. (2001). Multi-frequency seismic study of gas hydrate-bearing sediments in Lake Baikal, Siberia. *Marine Geology*, 172(1–2), 1–21. [https://doi.org/10.1016/s0025-3227\(00\)00117-1](https://doi.org/10.1016/s0025-3227(00)00117-1)
- Wallace, L., Barnes, P., Beavan, J., Van Dissen, R., Litchfield, N., Mountjoy, J., et al. (2012). The kinematics of a transition from subduction to strike-slip: An example from the central New Zealand plate boundary. *Journal of Geophysical Research*, 117. <https://doi.org/10.1029/2011jb008640>
- Watson, S. J., Mountjoy, J. J., Barnes, P. M., Crutchley, G. J., Lamarche, G., Higgs, B., et al. (2020). Focused fluid seepage related to variations in accretionary wedge structure, Hikurangi margin, New Zealand. *Geology*, 48(1), 56–61. <https://doi.org/10.1130/g46666.1>
- Weinberger, J. L., & Brown, K. M. (2006). Fracture networks and hydrate distribution at Hydrate Ridge, Oregon. *Earth and Planetary Science Letters*, 245(1–2), 123–136. <https://doi.org/10.1016/j.epsl.2006.03.012>
- Wood, W. T., Gettrust, J. F., Chapman, N. R., Spence, G. D., & Hyndman, R. D. (2002). Decreased stability of methane hydrates in marine sediments owing to phase-boundary roughness. *Nature*, 420, 656–660. <https://doi.org/10.1038/nature01263>
- Zoback, M. D. (2010). *Reservoir geomechanics*. Cambridge University Press.